Acta Materialia 148 (2018) 330–343

Contents lists available at ScienceDirect

Acta Materialia

journal homepage: www.elsevier.com/locate/actamat

Full length article

Defect-mediated vortex multiplication and annihilation in ferroelectrics and the feasibility of vortex switching by stress

Shuai Yuan [a, b, c], W.J. Chen [b, c], L.L. Ma [b, c], Ye Ji [b, c], W.M. Xiong [b, c], J.Y. Liu [b, c], Y.L. Liu [a, ***], Biao Wang [b, **], Yue Zheng [a, b, c, *, 1]

[a] School of Engineering, Sun Yat-sen University, Guangzhou, 510275, China
[b] State Key Laboratory of Optoelectronic Materials and Technologies, School of Physics, Sun Yat-sen University, 510275, Guangzhou, China
[c] Micro & Nano Physics and Mechanics Research Laboratory, School of Physics, Sun Yat-sen University, 510275, Guangzhou, China

A R T I C L E I N F O

Article history:
Received 24 August 2017
Received in revised form
16 January 2018
Accepted 16 January 2018
Available online 1 February 2018

Keywords:
Ferroelectrics
Vortex
Mechanical switching
Defect engineering

A B S T R A C T

The possibility of switching the direction of the dipole toroidal moment in ferroelectrics provides exciting opportunities for development of novel nanoscale memory and logic devices. However, a practical control of vortex chirality is rather challenging at present stage, not to mention via mechanical methods. In this paper, we performed the phase-field simulations to show that mechanical switching of vortex chirality can be achieved in ferroelectric nanoplatelet via defect engineering. After introducing a void defect in the nanoplatelet, relative stability of single-vortex state and multi-vortices state is found to be altered. Importantly, during stress-induced vortex multiplication process, the void is a favored nucleation core of new vortex; meanwhile, vortices tend to annihilate away from the void during a vortex annihilation process. As the favored regions of vortex nucleation and annihilation are not the same, a deterministic mechanical switching of vortex chirality can be achieved. The effects of temperature, shape of the nanoplatelet, void size, as well as void position, on the defect-mediated vortex switching behaviors are systematically revealed. Our study demonstrates the feasibility of vortex switching by mechanical loads and provides a route to control and develop electromechanical devices based on ferroic vortices.

1. Introduction

Ferroelectric materials are attracting increasing attention due to a wide spectrum of functional properties, such as dielectric, piezoelectric, pyroelectric, and ferroelectric properties, etc., as well as the formation of nanoscale domain structures. It is promising to take advantage of these properties in manufacturing advanced functional electronic, optoelectronic, and mechatronic devices. In particular, low dimensional ferroelectrics have been the objects under intense research during the past decade, for their novel or abnormal properties in comparison with bulk counterparts. For example, topological dipole states or domain structures, with vortex domain structure (VDS) being the well-known representative (in which the electric dipoles arrange a closure pattern and a chirality appears), are found to form in low dimensional ferroelectrics [1–6] and are attracting much attention due to the potential applications in high-density memory "bits" applications [1,3,7]. The formation of VDS in low dimensional ferroelectrics is due to a poor screening of the polarization charges at the surfaces. The stabilization of VDS in poor screening systems is attractive as it has long been thought that depolarizing effect would drive the system to be paraelectric. For the small size (typically < 10 nm) and a series of novel static and dynamic properties, including a variety of exotic states [8–10], vortex-polar transformation caused by electric field [11–13], vortex multiplication and annihilation behaviors induced by mechanical loads [14,15], superior electromechanical response due to vortex-polar coupling [16,17], etc., ferroelectric VDS holds tremendous promise for future applications.

In particular, the possibility of controlling the chirality of ferroelectric VDS opens exciting opportunities for development of novel nanoscale memory and logic devices. However, a practical

* Corresponding author. School of Engineering, Sun Yat-sen University, Guangzhou, 510275, China.
** Corresponding author.
*** Corresponding author.
E-mail addresses: stslyl@mail.sysu.edu.cn (Y.L. Liu), wangbiao@mail.sysu.edu.cn (B. Wang), zhengy35@mail.sysu.edu.cn (Y. Zheng).
[1] Permanent address: State Key Laboratory of Optoelectronic Materials and Technologies, School of Physics, Sun Yat-sen University, 510275, Guangzhou, China.

https://doi.org/10.1016/j.actamat.2018.01.018
1359-6454/

control of the chirality of ferroelectric VDS is rather challenging, due to the fact that the dipole toroidal moment is conjugate to the curl of **E** but not to a uniform electric field [18]. A control of the vortex chirality by curled electric fields has been modeled [12]. However, it is difficult to generate and apply a nanoscale curled field in practice. Alternatively, homogeneous electric field has been proposed to switch vortex chirality in asymmetric ferroelectric nanodisks [19] and in a dot-film system [20]. A strategy of vortex switching which utilizes mechanical loads (e.g., making use of the dislocation stress field or AFM tip loading field) to impose an 'extrinsic' asymmetry to the ferroelectric nanostructures, has also been proposed [21]. As a consequence, even for systems with a high geometric symmetry, vortex switching can be realized by a homogeneous electric field as well.

Investigations of vortex switching in ferroelectrics so far are focused on electrical switching, i.e., via the application of electric fields. However, for electrical switching, the electric fatigue and aging behavior of ferroelectrics are almost inevitable problems [22–25]. Considering the well-known coupling between polarization and strain/stress, it is fundamental to ask if vortex switching can be also realized via the application of mechanical loads. On the one hand, polarization couples with electrical field in odd symmetry whereas it couples with strain or stress in even symmetry. It is expected that the mechanism of mechanical switching of vortex (if exists) should be quite different from that of electrical switching. On the other hand, vortex switching is likely to occur via a nucleation/annihilation mechanism, i.e., with the forming of new vortex (vortices) in opposite chirality to the initial state and the disappearing of old vortex (vortices). Not only electric fields but also mechanical loads can lead to the nucleation and annihilation of vortex [14,15]. This indicates a possibility of vortex switching via mechanical loads. Without the use of electric field, mechanical switching of vortex provides a novel route to control VDSs and should be also significant for the development of mechanical logic devices based on VDSs. Nevertheless, to the best of our knowledge, the feasibility of vortex switching by mechanical loads and its regularity has not been demonstrated and discussed before.

In this paper, by performing the phase-field simulations, we demonstrate a mechanical switching mechanism to control the vortex chirality in ferroelectric nanoplatelet (FNPL) via defect engineering. A void defect is introduced in the FNPL. Acting as an artificial vortex core, such a void defect is found to affect not only the stability of vortex states but also the stress-induced vortex multiplication and annihilation behavior in the FNFL. Consequently, a deterministic switching of vortex chirality can be realized after a stress-loading/unloading process. We systematically summarized the effects of temperature, shape of the nanoplatelet, void size, and void position, on the defect-mediated vortex switching behaviors. Our results demonstrate the feasibility of vortex switching via mechanical loads and should be instructive for the practical control and applications of ferroelectric VDS.

2. Phase-field model

A phase-field model is adopted to capture the characteristic of ferroelectric VDS in FNPLs subjected to external mechanical loads. According to the previous works [26–29], we choose the spontaneous polarization field $\mathbf{P} = (P_1, P_2, P_3)$ as the order parameter to represent the domain structure. The electric displacement $\mathbf{D}$ is expressed as,

$$\mathbf{D} = \varepsilon_0\mathbf{E} + \boldsymbol{\chi}_\mathbf{b}\cdot\mathbf{E} + \mathbf{P} = \boldsymbol{\varepsilon}_\mathbf{b}\cdot\mathbf{E} + \mathbf{P} \tag{1}$$

where $\mathbf{E}$ is the electric field, ε_0 is the vacuum dielectric constant, $\boldsymbol{\chi}_\mathbf{b}$ and $\boldsymbol{\varepsilon}_\mathbf{b}$ are the background permittivity tensor and dielectric constant tensor, respectively.

The total free energy of system, which is a functional of the order parameter $\mathbf{P}$, is expressed as a sum of bulk Landau energy, gradient energy, elastic energy, electrostatic energy and surface energy, i.e.,

$$F(\mathbf{P}, \nabla\mathbf{P}, \boldsymbol{\varepsilon}) = \int_V \left[f_{\mathrm{Land}}(\mathbf{P}) + f_{\mathrm{elas}}(\mathbf{P}, \boldsymbol{\varepsilon}) + f_{\mathrm{grad}}(\nabla\mathbf{P}) + f_{\mathrm{elec}}(\nabla\mathbf{P})\right]\mathrm{d}V + \int_S f_{\mathrm{surf}}(\mathbf{P})\mathrm{d}S \tag{2}$$

where f_{Land}, f_{elas}, f_{grad}, and f_{elec} are densities of bulk Landau energy, gradient energy, elastic energy, electrostatic energy and surface energy, respectively. $\nabla\mathbf{P}$ denotes the gradient tensor of the polarization field, $\boldsymbol{\varepsilon}$ is total strain tensor. V is the volume, and S is surface of the system.

The bulk Landau energy density f_{Land} describes the ferroelectric transition of the bulk material. It is written as a Taylor series expansions in powers of the spontaneous polarization. For a ferroelectric with a cubic paraelectric phase, such as $PbTiO_3$ (PTO), a sixth-order polynomial of the spontaneous polarization is usually adopted [30],

$$f_{\mathrm{Land}} = a_1\sum_i P_i^2 + a_{11}\sum_i P_i^4 + a_{12}\sum_{i>j} P_i^2P_j^2 + a_{111}\sum_i P_i^6 + a_{112}\sum_{i>j}\left(P_i^4P_j^2 + P_j^4P_i^2\right) + a_{123}\prod_i P_i^2 \tag{3}$$

where a_1, a_{11}, a_{12}, a_{111}, a_{112} and a_{123} are phenomenological coefficients, and i and j are indexes ranging from 1 to 3. Coefficient a_1 satisfies the Curie-Weiss law and depends on temperature linearly.

Due to inhomogeneous polarization field of the ferroelectric domain structure, the gradient energy term f_{grad} is included to the total free energy of system. To the lowest order of Taylor expansion, it can be written in the tensor form as follows,

$$f_{\mathrm{grad}} = \frac{1}{2}\nabla\mathbf{P}\mathbf{:}\mathbf{g}\mathbf{:}\nabla\mathbf{P} \tag{4}$$

where $\mathbf{g}$ is the fourth-order tensor of gradient energy coefficient. For ferroelectrics with a cubic paraelectric phase, there are only three independent components of $\mathbf{g}$, i.e., g_{11}, g_{14}, and g_{44}, with their subscripts written according to Voigt notations [31].

According to Khachaturyan's microscopic elastic theory [32], the elastic energy is contributed by the strains that can produce stresses, which are originated from the incompatibility of the eigenstrains (e.g., those from the ferroelectric domains), and from the elastic deformation caused by the external force. Therefore, f_{elas} can be described by the following tensor form,

$$f_{\mathrm{elas}} = \frac{1}{2}\mathbf{e}\mathbf{:}\mathbf{C}\mathbf{:}\mathbf{e} = \frac{1}{2}\left(\boldsymbol{\varepsilon} - \boldsymbol{\varepsilon}^0\right)\mathbf{:}\mathbf{C}\mathbf{:}\left(\boldsymbol{\varepsilon} - \boldsymbol{\varepsilon}^0\right) \tag{5}$$

where $\mathbf{C}$ being the fourth-order tensor of elastic stiffness; $\mathbf{e}$ and $\boldsymbol{\varepsilon}^0$ are the second-order tensors of elastic strain and eigenstrain, respectively. The eigenstrain tensor $\boldsymbol{\varepsilon}^0$ caused by the ferroelectric domains is related to the polarization as $\boldsymbol{\varepsilon}^0 = \mathbf{P}\cdot\mathbf{Q}\cdot\mathbf{P}$, with $\mathbf{Q}$ being the fourth-order tensor of electrostrictive coefficient. For a ferroelectric with a cubic paraelectric phase, there are only three nonzero components of $\mathbf{C}$ and $\mathbf{Q}$, i.e., C_{11}, C_{12}, C_{44} and Q_{11}, Q_{12}, Q_{44}, with their subscripts written according to Voigt notations.

Due to the Coulomb interaction of electric dipoles, the electrostatic energy should be considered. Based on the continuum theory [27,35], the electrostatic energy density f_{elec} is expressed as,

$$f_{\mathrm{elec}} = -\mathbf{P}\cdot\mathbf{E} - \frac{1}{2}\mathbf{E}\mathbf{:}\varepsilon_b\mathbf{:}\mathbf{E} \tag{6}$$

Note that the sign here is negative as we are dealing with the Gibbs free energy rather than the internal energy. For a background material in cubic symmetry, the background dielectric tensor $\boldsymbol{\varepsilon}_{\mathrm{b}}$ has equivalent components in the three axis directions, i.e.,$\varepsilon_{\mathrm{b}} = \varepsilon_{11\mathrm{b}} = \varepsilon_{22\mathrm{b}} = \varepsilon_{33\mathrm{b}}$.

In addition, to take account of the polarization inhomogeneity across the surfaces, a surface energy term f_{surf} is included. Employing the so-called extrapolation lengthδ_i^{eff}, the surface energy density is written in a tensor form as,

$$f_{\mathrm{surf}} = \frac{1}{2}\mathbf{P}\cdot\boldsymbol{\omega}\cdot\mathbf{P} \tag{7}$$

where $\boldsymbol{\omega}$ is a surface coefficient tensor. Note, for simplicity, the asymmetry effect of surface is neglected, otherwise a first-order term should be added [36]. For ferroelectrics with a cubic paraelectric phase, we simply take $\boldsymbol{\omega} = \mathrm{diag}(\mathbf{D}_1^s/\delta_1^{\mathrm{eff}}, \mathbf{D}_2^s/\delta_2^{\mathrm{eff}}, \mathbf{D}_3^s/\delta_3^{\mathrm{eff}})$, with D_i^s being coefficients depending on the gradient energy coefficients and surface orientation [30].

Integrating the sum of free energy densities above over the entire volume and all the surfaces, the total free energy of the system can be obtained. The temporal evolution of the polarization field is described by the time-dependent Ginzburg-Landau (TDGL) equation,

$$\frac{\partial \mathbf{P}(\mathbf{r}, t)}{\partial t} = -L\frac{\delta F}{\delta \mathbf{P}(\mathbf{r}, t)} \tag{8}$$

where L is a kinetic coefficient related to the domain wall mobility and t is the time.

The boundary condition of polarization could be obtained mathematically with the application of the variation principle to the total free energy, i.e., $\delta F/\delta\mathbf{P} = 0$,

$$(\mathbf{g}\mathbf{:}\nabla\mathbf{P})\cdot\mathbf{n} + \boldsymbol{\omega}\cdot\mathbf{P} = \mathbf{0} \tag{9}$$

where $\mathbf{n}$ is the normal unit vector of a specific surface.

The mechanical and electrical fields are assumed to have much smaller relaxation times than that of polarization, so that the evolution of mechanical and electrical fields can be treated in an 'adiabatic' way. The mechanical and electrical equilibrium can be instantaneously reached once the polarization field changes. Under this approximation, the mechanical equilibrium equation is considered,

$$\nabla\cdot\boldsymbol{\sigma} = 0 \tag{10}$$

where $\boldsymbol{\sigma} = \mathbf{C}\mathbf{:}\mathbf{e}$ is the stress tensor. For FNPL subjected to external mechanical stress, the mechanical boundary condition is given by

$$\boldsymbol{\sigma}\cdot\mathbf{n}|_S = \boldsymbol{\tau}|_S \tag{11}$$

with $\boldsymbol{\tau}$ being the surface traction vector. In this work, a surface traction along x-axis τ is applied at the top and bottom surfaces of the FNPL, as shown in Fig. 1.

Moreover, to explore the possible formation of VDS, the system is assumed to be absent of free charges. The electrostatic equilibrium equation is adopted as follows,

$$\nabla\cdot\mathbf{D} = 0 \tag{12}$$

Meanwhile, an open-circuit condition is considered by setting $\mathbf{D}\cdot\mathbf{n} = 0$ at the surfaces of the system.

3. Numerical method

The TDGL equation [Eq. (8)] is solved numerically with the boundary condition [Eq. (9)] via an Euler iteration method after discretizing it both on time and space. At each time step of polarization evolution, the mechanical and electrical fields are obtained by the solutions of the mechanical and electrostatic equilibrium equations, i.e., Eqs. (10) and (12), together with the appropriate boundary conditions as mentioned above. Finite element method (FEM) is adopted to solve the mechanical and electrostatic equilibrium equations numerically.

In this study, we focus on FNPLs made of PTO. The results we obtained, however, are not confined to PTO. Similar behaviors are expected in other ferroelectric materials, such as BaTiO3, and even in soft magnetic materials that can form VDS considering the fact that formation of magnetic VDS is also driven by depolarization mechanism, and the key for the vortex switching–transformation behavior of vortex multiplication and annihilation induced by mechanical loads–has also been found in soft magnets [38,39]. As shown in Fig. 1, a Cartesian coordinate system is attached to the FNPL with the origin point of the coordinate system being located at the center of the FNPL, and x, y and z-axes parallel to the length, width and thickness direction of the FNPL, respectively. A void defect is introduced to the FNPL (Fig. 1b). We choose the default simulation dimensions of FNPL to be $l_a = 30$ nm, $l_b = 20$ nm, and $h = 4$ nm, the default shape of void to be circular, the default location of the void to be at the center of the FNPL, i.e., $(x_0, y_0) = (0, 0)$, and the default diameter D to be 4 nm, unless otherwise specified when the size and geometry effects are discussed. A three-dimensional (3D) discrete grid with a mix of cuboid and triangular prism elements is employed. The size of the smallest element is less than 0.4 nm. A default simulated temperature is set to be near room temperature, 300 K, unless otherwise specified when the temperature effect is discussed. Values of all the parameters used in this work are listed in Ref. [37]. Specifically, the expansion coefficients of the Landau energy, the elastic stiffness and the electrostrictive coefficients are from Ref. [33], the isotropic gradient coefficients are from Ref. [29], the extrapolation length is from Ref. [34], and the background dielectric constant is from Refs. [27] and [28]. In this paper, toroidization is adopted to characterize the chirality of the vortex states, i.e., $\mathbf{G} = V^{-1}\int_V \mathbf{R} \times (\mathbf{P} - \overline{\mathbf{P}})dV$, where $\mathbf{R}$ is the position vector, and $\overline{\mathbf{P}}$ is the average polarization of the system.

4. Results and discussion

We would first like to use a schematic to illustrate how a void defect modifies the stress-induced multiplication/annihilation behavior of a vortex state in FNPL, and how this can lead to a

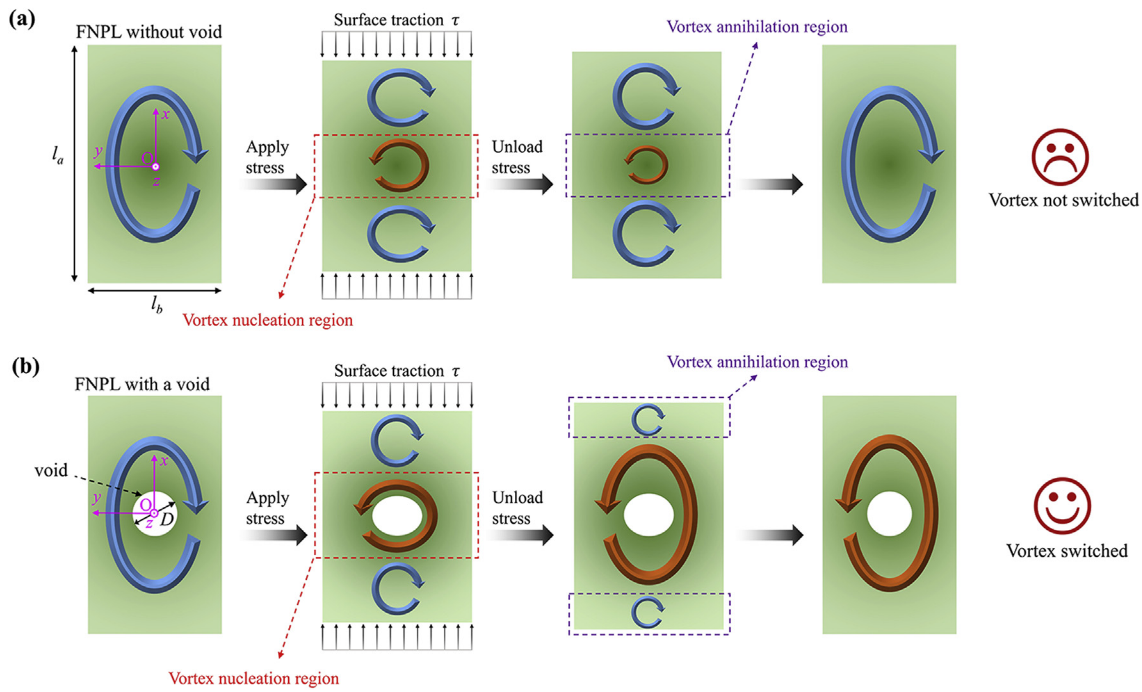

Fig. 1. A schematic illustrating the effect of a void on the transformation behavior of vortex states under external stress in FNPL. (a) Stress-induced transformation from a single-vortex state to multi-vortices state in FNPL without void. The vortex nucleation region and annihilation region are the same at the middle region of FNPL. (b) Stress-induced transformation from a single-vortex state to multi-vortices state in FNPL with a circular void. The vortex nucleation region is at the middle region, however, the vortex annihilation region is at the top and bottom region of FNPL.

deterministic switching of vortex chirality by stress. As shown in Fig. 1a, a FNPL without void is initially in a single-vortex state. Application of an x-axis compressive surface traction τ induces a transformation from the single-vortex state to a multi-vortices state (e.g., a 3-vortices state) in the FNPL. This vortex multiplication takes place via nucleation of a 'new' vortex at the middle region and splitting of the initial vortex into two vortices (we would like to call them 'old' vortices) at the top and bottom regions. Meanwhile, unloading of the surface traction (if the 3-vortices state is not stable at stress free condition) or applying a relative tensile surface traction leads to the re-formation of a single-vortex state, via the annihilation of the 'new' vortex at the middle region and the merging of the two 'old' vortices at the top and bottom. As both the favored vortex nucleation region and annihilation region are the same, i.e., at the middle region of the FNPL, the final single-vortex state has the same chirality with that of the initial state. The scenario, however, is different for FNPL with a void, where the favored vortex nucleation region and annihilation region are not at the same place (Fig. 1b). When the FNPL is under compressive stress, transformation from the single-vortex state to a 3-vortices state still occurs via the nucleation of a 'new' vortex at the middle region. However, after unloading of the surface traction or applying a tensile surface traction, a single-vortex state is re-formed via the annihilation of the top and bottom 'old' vortices. This happens due to that the void enhances the stability of the middle vortex, which is difficult to be annihilated. As a result, chirality of a single-vortex state in FNPL can be switched in a deterministic way via a stress loading/unloading process.

4.1. Vortex formation in FNPL with a void

Fig. 2a and b respectively depict the equilibrium distributions of polarization field in FNPLs without and with a circular void. The diameter of circular void is $D = 8$ nm. It can be seen that both FNPLs form a domain structure with the polarization field arranged in a closed-flux pattern, and parallel to the surfaces, due to the open-circuit boundary condition. Note that, due to the geometry and the size of the FNPL that we concerned, what formed in the FNPL is not ideal vortex (vortices) but flux-closure domain structure. In a general point of view, such flux-closure domain structure can be regarded as vortex-like domain structure. In this work, we simply refer it as VDS or vortex state. A careful look into the polarization field in the two FNPLs shows that the void modifies the polarization field around it. In contrast to the ideal single-vortex in FNPL without void (Fig. 2a), there are two small vortices (as heighted by the white dashed lines) located on both sides of the void along x-axis in FNPL with a void (Fig. 2b). These two small vortices are caused by a combining effect of the open-circuit condition at the void surface and the geometry incompatibility of the void and the FNPL. Moreover, in Fig. 2c, distributions of stress field components σ_{11} and σ_{22} in the two FNPLs are depicted. For the both FNPLs, the stress takes larger values near the vortex core than the other region. Note that while the void occupies a large part of the vortex core and thus removes the high stress therein, it also causes a significant stress concentration around it. Fig. 2d further depicts distributions of the gradient energy density f_{grad} and the elastic energy density f_{elas} of the two FNPLs. For FNPL without void, the two energy densities have larger values near the domain walls, especially near the vortex core. For FNPL with a void, a significant decrease of the two energy densities near vortex core is clearly seen. In fact, as the void is introduced to the FNPL, the total energy of the system decreases owing to the removal of the high energy region near the vortex core. As a result, a void defect enhances the stability of vortex states in the FNPL. This is similar to the observation in previous works that vortex state in a ring is more stable than in a disk [40,41]. In the following, it will be shown that the enhanced stability of vortex around the void defect is the key to stress-induced vortex switching.

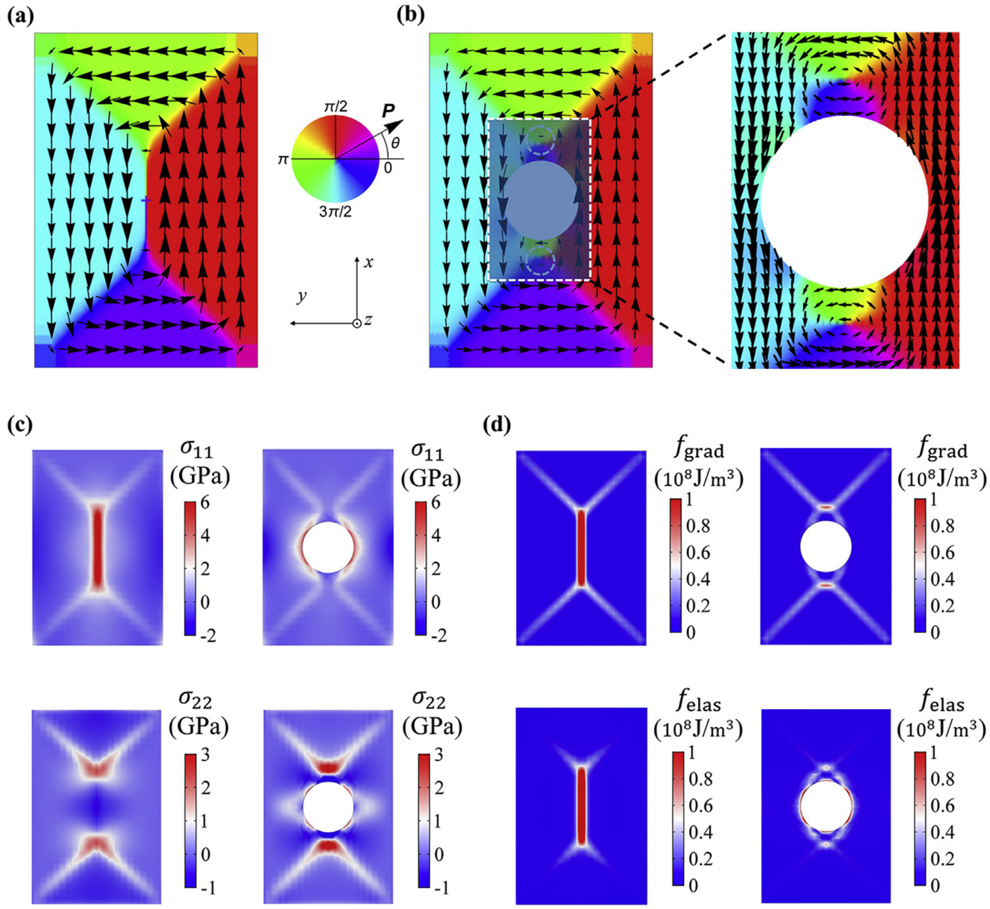

Fig. 2. Distribution of polarization field in *x-y* plane in FNPLs (a) without and (b) with a void under zero surface traction. The diameter of circular void is $D = 8$ nm. Different color stands for different orientations of polarization here. (c) Distributions of stress field of equilibrium single-vortex state in the two FNPLs. (d) Distributions of gradient and elastic energy density of equilibrium single-vortex state in the two FNPLs. (For interpretation of the references to color in this figure legend, the reader is referred to the Web version of this article.)

In practice, for FNPLs with a not too small size or at a relatively low temperature, single-vortex state, together with multi-vortices states with different number of vortices (e.g., 2- or 3-vortices states), can be stabilized in the FNPL. It is interesting to ask how a void defect modifies the stabilization of different vortex states in FNPL. To see this, the formation probability of single-vortex and multi-vortices states in FNPL without void and in FNPLs with a void of circular, triangular or square shape are simulated and compared. Simulations with over 100 sets of initial random polarization perturbation are performed in order to obtain a statistics analysis for each FNPL at given temperature. The random polarization perturbation obeys the Gaussian distribution with a zero mean polarization and a standard derivation being 10^{-4} C/m^2. Fig. 3a depicts the evolution snapshots of forming a counterclockwise (CCW) single-vortex state in the four FNPLs at $T = 300$ K. Note that the evolution proceeds with nucleation, growth and merging of dipole vortices. The vortex nucleation sites are quite different in the four FNPLs due to the different random perturbations. Moreover, dipole vortices tend to nucleate outside the void rather than around it at the beginning stage. This is counterintuitive at the first glance as structural defects are expected to be favored vortex nucleation sites. Actually, this is due to the fact that the void size is not small enough to be the vortex nucleation site, in contrast to the case of lattice defects such as dislocations [21]. Nevertheless, as the void exerts an open-circuit condition at the void surface, it strongly modifies the dipole behavior around it and consequently affects the overall evolution of VDS.

Corresponding to the evolution shown in Fig. 3a, we depict in Fig. 3b the evolution curves of toroidization component G_z as a function of time at 300 K for the four FNPLs. It shows that the evolution towards the stable single-vortex state tends to take a longer time for FNPL without void than FNPLs with a void. Moreover, toroidization of the single-vortex state in FNPLs with a void has larger values than that in FNPL without void. This is mainly due to that the vortex core region, a large part of which are removed by the void, has a smaller contribution to the total toroidal moment than the outer region.

We summarize in Fig. 3c the statistics of formation probability of single-vortex and multi-vortices states in FNPLs without void and with voids in different shapes at $T = 200$ K and 300 K. The formation probability of single-vortex state in FNPL without void is approximately 73% and 77% at $T = 200$ K and 300 K, respectively. Meanwhile, the probability increases to 85% (91%), 89% (92%), and 90% (94%) in FNPLs with a circular, square and triangular void at $T = 200$ K (300 K), respectively. Clearly, through introducing a void defect in the FNPL, the single-vortex state is more favored to form. On the one hand, the polarization field tends to rotate around the void to form a pinned vortex, which reduces the probability of forming other polarization configuration near the void. On the other hand, as the void removes the high energy region near the vortex core, the stability of the pinned vortex is enhanced, which depresses the living space of other vortices in the rest region of the

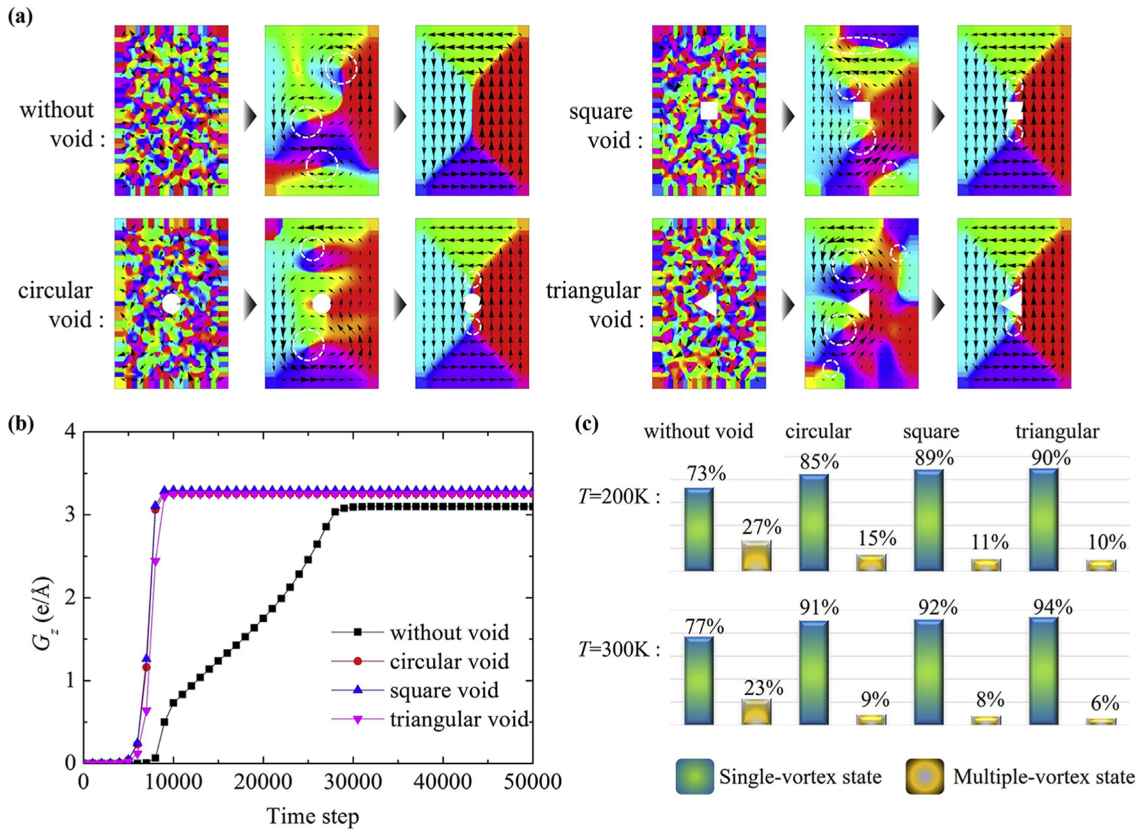

Fig. 3. Formation of single-vortex state in FNPL with different shapes of void at the center. (a) The evolution snapshots from initial random polarization perturbation to a single-vortex state in FNPLs without void and with a circular, square, and triangular void in the center, respectively. The simulated temperature is $T = 300$ K. (b) The evolution curve of toroidization G_z as a function of time at $T = 300$ K. (c) Probability of single-vortex and multi-vortices formation in FNPLs with different shapes of void at $T = 200$ K and 300 K.

FNPL. The enhanced stability of single-vortex state should be useful if we want this state in practical applications.

4.2. Stress-induced vortex switching in FNPL with a void at the center

The vortex multiplication and annihilation behaviors and the feasibility of stress-induced vortex switching in FNPL with a void at the center is investigated in this section. We simulate the evolution of a single-vortex state in FNPL without void and in FNPL with a void subjected to a stress loading/unloading process at $T = 300$ K. Specifically, the two FNPLs are set to adopt a CCW single-vortex state at the initial state, which is relaxed to equilibrium. A compressive surface traction $\tau = -3$ GPa is then applied to the FNPLs so that a vortex multiplication process occurs. After reaching a steady state, the stress traction is then removed to trigger a vortex annihilation process and a single-vortex state is reformed. Snapshots of the VDS evolution of the two FNPLs are depicted in Fig. 4a and b, respectively, and the evolution curves of the toroidization component G_z are shown in Fig. 4c. One can see that, for both FNPLs, the initial CCW single-vortex state evolves into a 3-vortices state under the stress loading via the nucleation of a clockwise (CW) vortex at the middle region. This is accompanied with the decrease of the toroidization component G_z. A single-vortex state is re-formed for both FNPLs during the stress-unloading process. However, the evolution paths are quite different. For FNPL without void, by removal of the compressive stress, the nucleated CW vortex becomes unstable and shrinks, and the two CCW vortices at the top and bottom expands and gradually merge into a CCW vortex in the whole FNPL. In contrast, for FNPL with a void, the CW vortex expands after the removal of stress, and the two CCW vortices on both sides become smaller and finally vanish at the surfaces. As a result, the final vortex state of FNPL without void is still CCW, whereas for FNPL with a void, the final vortex state is CW, which is opposite to the initial state. The toroidization curves also clearly indicate the stress-induced vortex switching (Fig. 4c). As what we have already illustrated in Fig. 1, such a stress-induced vortex switching is deterministic rather than stochastic as the void alters the vortex nucleation (on the loading) and annihilation (on the unloading) process in a definite way. On the loading process, 'new' vortex with opposite chirality nucleates at the middle region of the FNPL, due to the fact that the polarization field at the middle region is against the compressive stress field and that void also has a stress concentration effect, which together make the polarization field at the middle region much easier to be changed. Meanwhile, during the unloading stage, a single-vortex state is re-formed via the annihilation of the top and bottom 'old' vortices. This happens due to that the void enhances the stability of the middle vortex (as the void surface enforces an open-circuit-like boundary condition), which is difficult to be annihilated. Consequently, chirality of a single-vortex state in FNPL can be switched in a deterministic way via a stress loading/unloading process.

At relatively low temperature condition, FNPL might maintain a multi-vortices state after a stress loading/unloading process. For this situation, vortex switching can still occur in FNPL with a void, if a tensile stress is further applied to the FNPL so that the multi-vortices state transforms back to the single-vortex state. To see this, we simulate the evolution of a CCW single-vortex state in FNPL without void and in FNPL with a void at $T = 100$ K. At the first stage, the FNPLs are subjected to a compressive stress loading/unloading

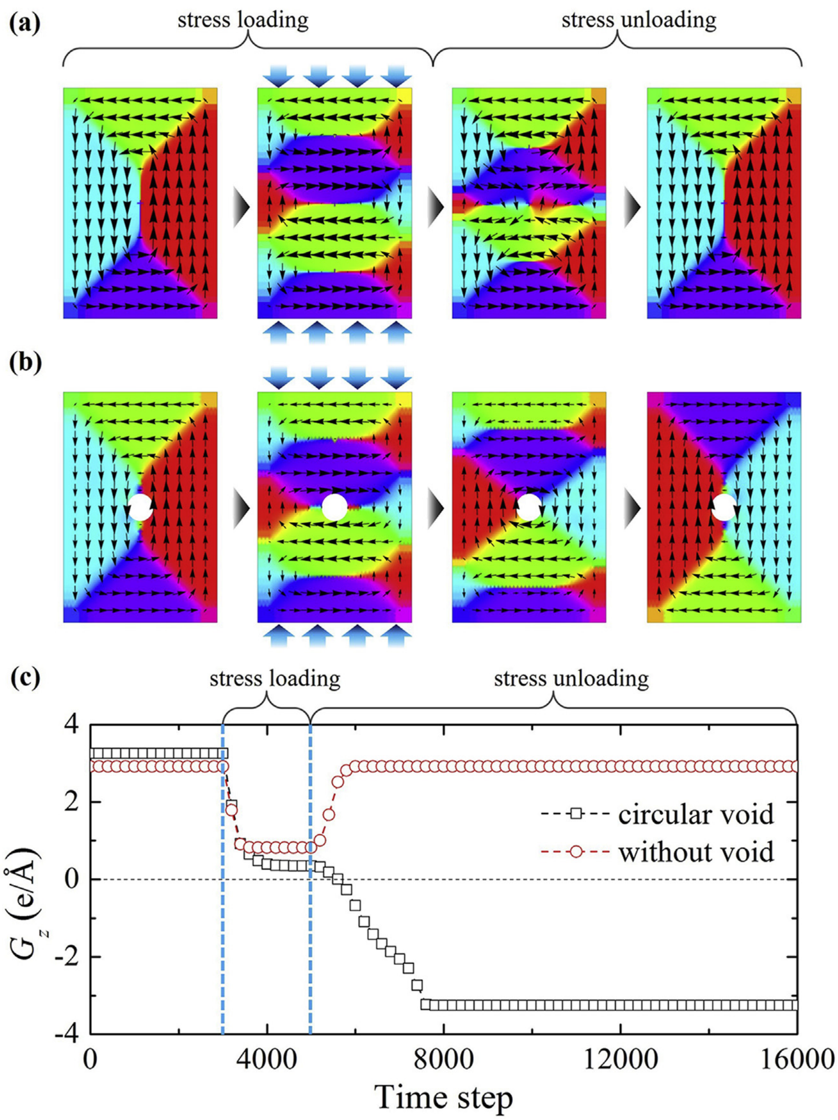

Fig. 4. Evolution of a single-vortex state in FNPL without void and in FNPL with a void subjected to a stress loading/unloading process at $T = 300$ K. (a), (b) Snapshots of the VDS evolution of the two FNPLs. (c) Evolution curves of the toroidization component G_z of the two FNPLs.

process with $\tau_1 = -3$ GPa. As shown by the snapshots of the VDS evolution in Fig. 5a and b for the two FNPLs, respectively, this process transforms the initial single-vortex state into a 3-vortices state in both FNPLs. At the second stage, the FNPLs are subjected to a tensile stress loading/unloading process with $\tau_2 = 1$ GPa. A single-vortex state is reformed after this process for both FNPLs. However, similar to the previous case at room temperature (Fig. 4), the final vortex state of FNPL without void is the same as the initial state, whereas the final vortex state of FNPL with a void is opposite to the initial state. This is also clearly seen in the toroidization curve (Fig. 5c).

In general, for a single-vortex state in FNPL with a void subjected to a compressive stress loading/unloading process at a given surface traction and temperature condition, three kinds of evolution paths can be expected. The first path is that the single-vortex state would not transform into a multi-vortices state as the surface traction τ is below τ_c [14], and therefore vortex switching does not occur. The second path is that the single-vortex state transforms into a multi-vortices state as the surface traction τ is above τ_c, and after the removal of stress, the multi-vortices state is transformed into a single-vortex state. Accompanying with this path, vortex switching occurs if the final single-vortex state has an opposite chirality to the initial state. This kind of vortex switching has already been demonstrated in Fig. 4, with the multi-vortices state being a 3-vortices state. In the following, we would like to define it as Type-I switching. The third path is that the single-vortex state transforms into a multi-vortices state as the surface traction τ is above τ_c, and the multi-vortices state is maintained after the stress unloading. In this case, vortex switching might occur when a tensile stress is further applied so that the multi-vortices state transforms back to a single-vortex state, as what we have shown in Fig. 5, where the multi-vortices state is a 3-vortices state. We would like to define it as Type-II switching.

To see the three paths and the possible vortex switching clearly, in Fig. 6a and b, we depict the toroidization component G_z as a function of time for a single-vortex state in FNPL with a void subjected to a stress loading/unloading process at various surface traction and temperature conditions. Specifically, the three cases shown in Fig. 6a are at $T = 300$ K but at different values of surface traction whereas shown in Fig. 6b are at $\tau = -2.2$ GPa but at

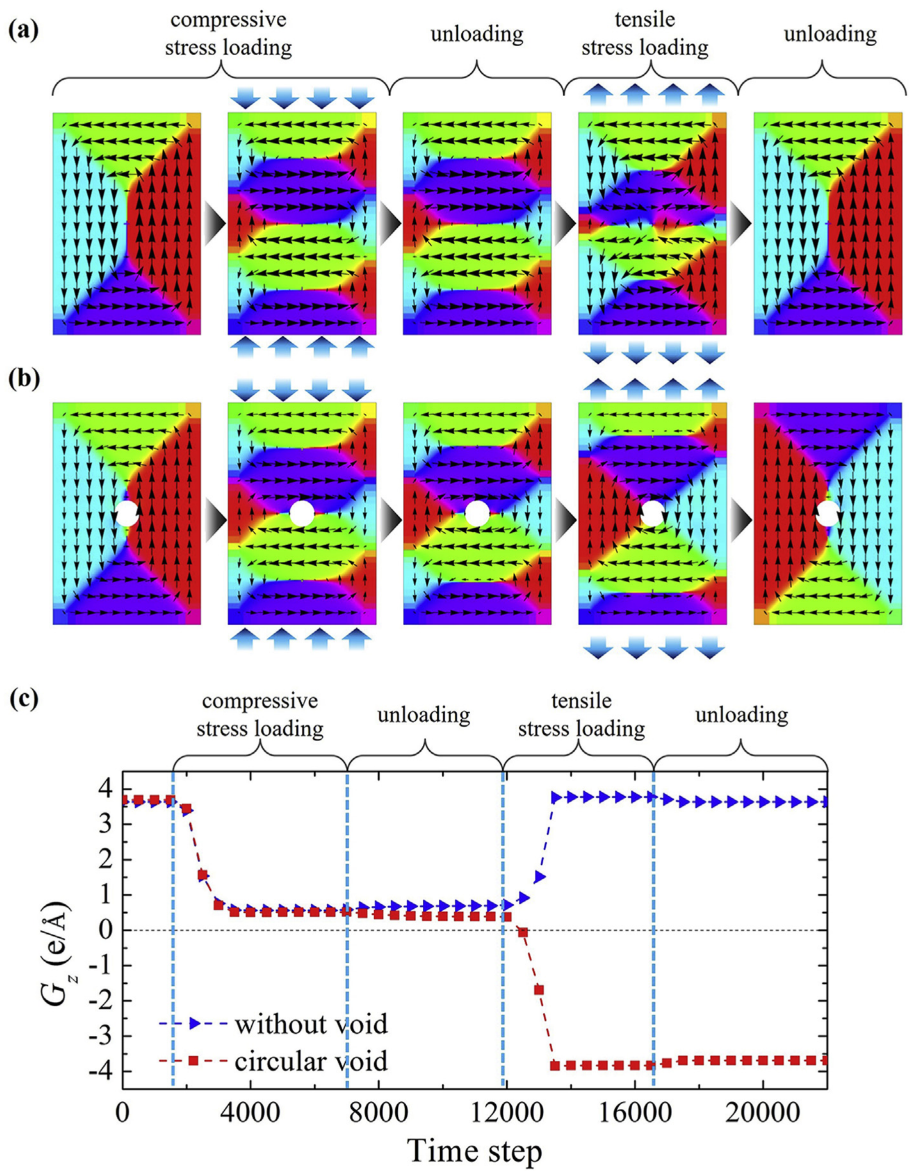

Fig. 5. Snapshots of the VDS evolution of a single-vortex state (a) in FNPL without void and (b) in FNPL with a void at $T = 100$ K under a compressive stress loading/unloading process followed by a tensile stress loading/unloading process. (c) The evolution curves of the toroidization component G_z of the two FNPLs.

different temperatures. From Fig. 6a, one can see that the first path occurs at $\tau = -1.0$ GPa and -1.5 GPa, and the second path accompanying with Type-I switching occurs at $\tau = -2.0$ GPa, indicating that there is a critical surface traction τ_c in between -2.0 GPa and -1.5 GPa. The temperature dependence of the evolution path is clearly seen in Fig. 6b. The second, the third and the first paths occur at $T = 300$ K, 100 K and 0 K, respectively. Note that, for the third path, vortex switching does not occur unless we further exert a tensile stress loading/unloading process.

In Fig. 6c, we plot a phase diagram which summarizes the feasibility of chirality switching of a single-vortex state in FNPL with a void subjected to a compressive stress loading/unloading process at different surface traction and temperature conditions. One can see that the feasibility of vortex switching depends on the temperature and surface traction, due to the different evolution paths as mentioned above. The ‘unswitching’, Type-I switching, and Type-II switching behaviors is associated with the first, the second and the third paths, respectively. Type-I switching occurs when the temperature is higher than 100 K. At temperature lower than 100 K, Type-II switching instead of Type-I switching would occur. The trend that the critical surface traction τ_c decreases as temperature increases is clearly seen.

4.3. Effect of void size on vortex switching

In the following, we would like to reveal effects of some factors that can modify the feasibility of the stress-induced vortex switching, which should be of both scientific and engineering significance. On the one hand, it is fundamental to ask how the strategy of defect-mediated vortex switching works well in different conditions. On the other hand, in practice, phase diagrams that predicting the proper range of conditions where vortex switching is feasible should be necessary for experimentalists who are interested on verifying our idea. At the first glance, there should exist a suitable void size beyond which vortex switching fails. When the void is small enough, its effect should be small. An increase of void size could enhance the stability of the vortex around it and lead to more feasible switching. However, when the void is

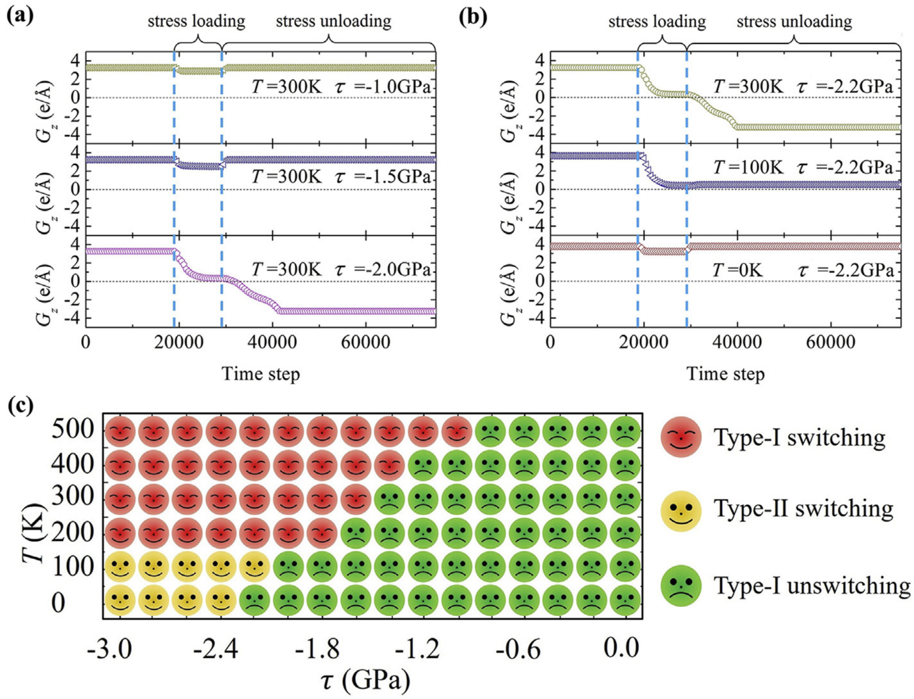

Fig. 6. The toroidization component G_z as a function of time for a single-vortex state in FNPL with a void subjected to a stress loading/unloading process at various surface traction and temperature conditions. (a) $\tau = -1.0, -1.5, -2.0$ GPaand $T = 300$ K. (b) $T = 300$ K, 100 K, 0 K and $\tau = -2.2$ GPa. (c) Phase diagram summarizing the feasibility of chirality switching of a single-vortex state in FNPL with a void subjected to a compressive stress loading/unloading process at different surface traction and temperature conditions.

large enough, as the width of the FNPL is finite, vortex nucleation around the void is expected to be difficult. To see this, the evolution of a single-vortex state in FNPLs with voids of various diameters during a stress loading/unloading process is simulated. Snapshots of the VDS evolution for four FNPLs with the void diameter being $D = 1$ nm, 8 nm, 15 nm and $D = 19$ nm at room temperature are shown in Fig. 7a–d, respectively. The loading stress τ is chosen to be -3.0 GPa for all FNPLs. It can be seen that FNPL with the void diameter being $D = 8$ nm exhibit Type-I switching, similar to that shown in the previous FNPL with $D = 4$ nm. Meanwhile, FNPLs with the void diameter being $D = 1$ nm and 15 nm maintain a multiple-vortices state after unloading indicating a feasibility of Type-II switching. A further loading of a slight tensile stress indeed transforms such state into a single-vortex state with opposite chirality to the initial state (Fig. 7a and b). Note that the reason why FNPLs with void diameter being $D = 1$ nm and 15 nm both can maintain a multiple-vortex state are not exactly the same, although both are due to a balance of the relative stability of the nucleated vortex around the void and the other two vortices. In the former FNPL, the enhanced stability of the nucleated vortex around the void is not strong enough to squeezing out the space of the other two vortices as the void size is quite small; in the latter FNPL, as the width of the FNPL is finite, the large void decreases the space of the nucleated vortex around the void and hence its stability. Moreover, for FNPL with the void diameter being $D = 19$ nm, as the lateral width of the FNPL at the middle is quite small, both the top and bottom regions forming a stable vortex. Vortex nucleation around the void does not occur during the stress loading, leading to a failure of vortex switching.

We calculate the critical surface traction τ_c of Type-I switching as a function of void diameter and temperature, as depicted in Fig. 7e and f, respectively. It can be seen that the vortex switching needs a smaller surface traction when the void is larger or the temperature is higher. When the void size is fixed, τ_c decreases as the temperature rises, due to that a higher temperature leads to easier nucleation of vortex. Meanwhile, at fixed temperature, τ_c decreases as the void size increases. Such a negative correlation between τ_c and the void size indicates that a larger void size leads to an easier nucleation of vortex. Such an easier nucleation of vortex is attributed to the stress concentration effect: as the void size increases, the lateral width of the FNPL at the middle becomes smaller and the stress therein becomes larger. Nevertheless, this trend can only keep in a moderate range of size. As already shown in Fig. 7d, when the void is large enough, vortex nucleation around the void would become difficult.

Moreover, Fig. 7e depicts a phase diagram which summarizes the feasibility of chirality switching of a single-vortex state in FNPLs with a void of various diameters subjected to a stress loading/unloading process and different temperature conditions. The loading stress τ is chosen to be -3.0 GPa for all FNPLs. One can see that Type-I switching is feasible for most of the void sizes and temperatures we have chosen. With the increase of temperature, the range of void size for Type-I switching increases. When the void size is beyond the range of void size for Type-I switching, Type-II switching can occur. With the decrease of temperature, the range of void size for Type-II switching increases. Unswitching only occurs at the extreme cases where the void is very small or very large.

4.4. Effect of width-length ratio of FNPL on vortex switching

We further consider the effect of width-length ratio of FNPL on the feasibility of stress-induced vortex switching. In the investigation of this section, we keep the lateral size of FNPLs to be $l_a l_b = 600$ nm^2, but change the width-length ratio $\eta = l_b/l_a$ of FNPLs from 0.2 to 1.0. Snapshots of the VDS evolution for four FNPLs with a void subjected to a stress loading/unloading process at room temperature are shown in Fig. 8a–d, with η being 0.4, 1.0, 0.8 and 0.6, respectively. The loading stress τ is chosen to be -3.0 GPa for all FNPLs. One can see that the evolution paths are quite different in the four FNPLs, indicating a strong effect of the width-length ratio.

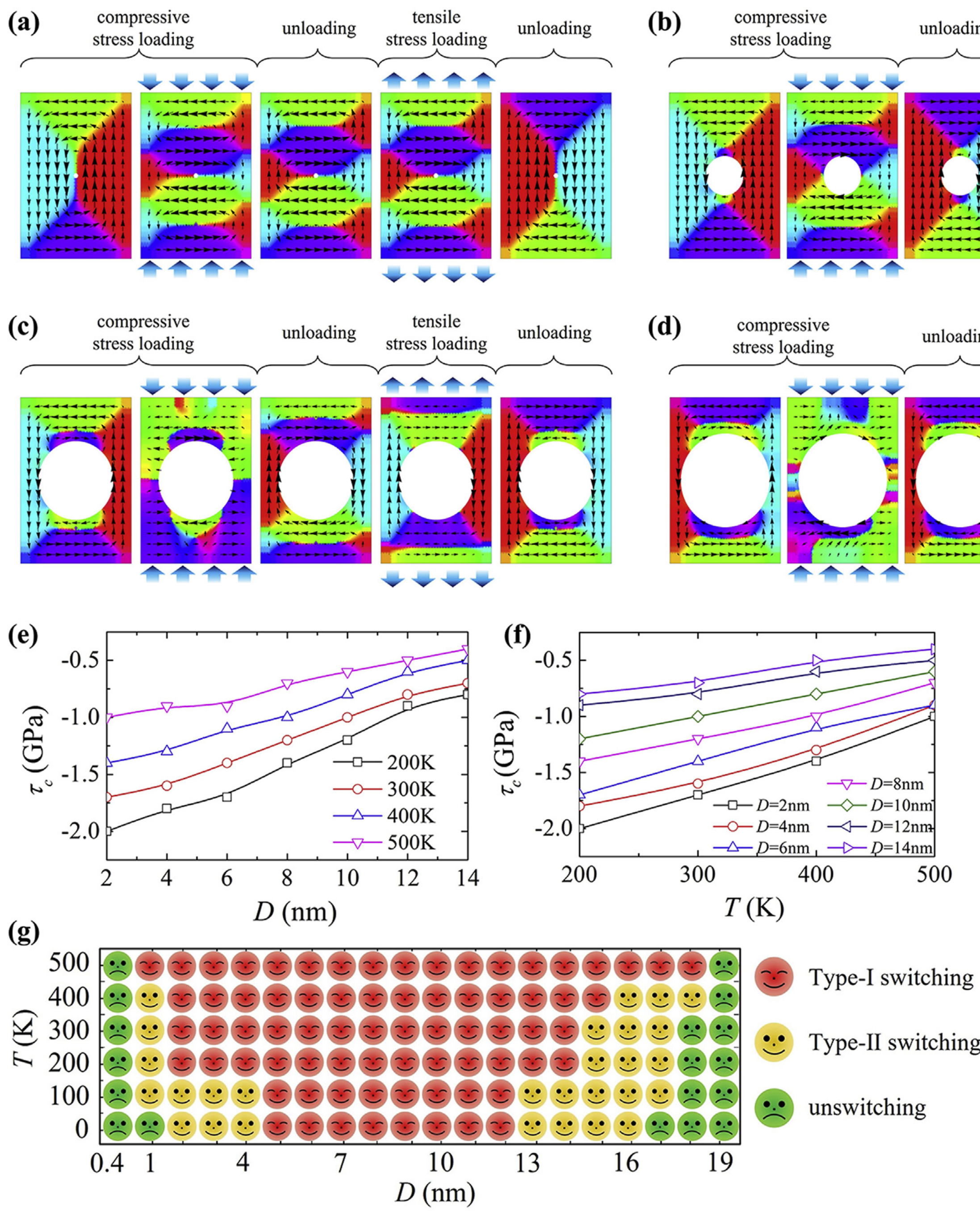

Fig. 7. Snapshots of the VDS evolution for four FNPLs with different void diameter during a compressive stress loading/unloading process at room temperature. (a) $D = 1$ nm, (b) 8 nm, (c) 15 nm, and (d) 19 nm. In (a) and (c), VDS evolution under a further tensile stress loading/unloading process is also depicted. Critical surface traction τ_c of Type-I switching as a function of (e) void diameter and (f) temperature. (g) Phase diagram summarizing the feasibility of chirality switching of a single-vortex state in FNPLs with a void of various diameters subjected to a stress loading/unloading process and different temperature conditions. The loading stress τ is chosen to be -3.0 *GPa*for all FNPLs.

Type-I switching occurs in FNPL with $\eta = 0.6$, accompanying with transformation of the single-vortex state to a 3-vortices state and back to a single-vortex state (Fig. 8d). For FNPL with $\eta = 0.4$, transformation of the single-vortex state to a 4-vortices state and back to a 2-vortices state is observed after a stress loading/unloading process (Fig. 8a). In the 4-vortices state, there are two new vortices with opposite chirality to the initial vortex state. One of them is nucleated around the void. As the stress is removed, these two vortices merge into a single-vortex by swallowing the vortex among them, forming a 2-vortices state in the whole FNPL. A further application of tensile stress can transform the 2-vortices state into a single-vortex state with opposite chirality to the initial state, thus vortex switching (Type-II) occurs. Note that 3-vortices state can be formed instead of 4-vortices state this FNPL at smaller surface traction, while 5-vortices state can be formed at higher surface traction. Both cases can lead to Type-II switching. Actually, FNPLs with a smaller width-length ratio tend to exhibit more fruitful switching modes, as they can undergo more fruitful vortex multiplication behaviors as a function of the surface traction.

For FNPL with $\eta = 0.8$, the single-vortex state transforms into a

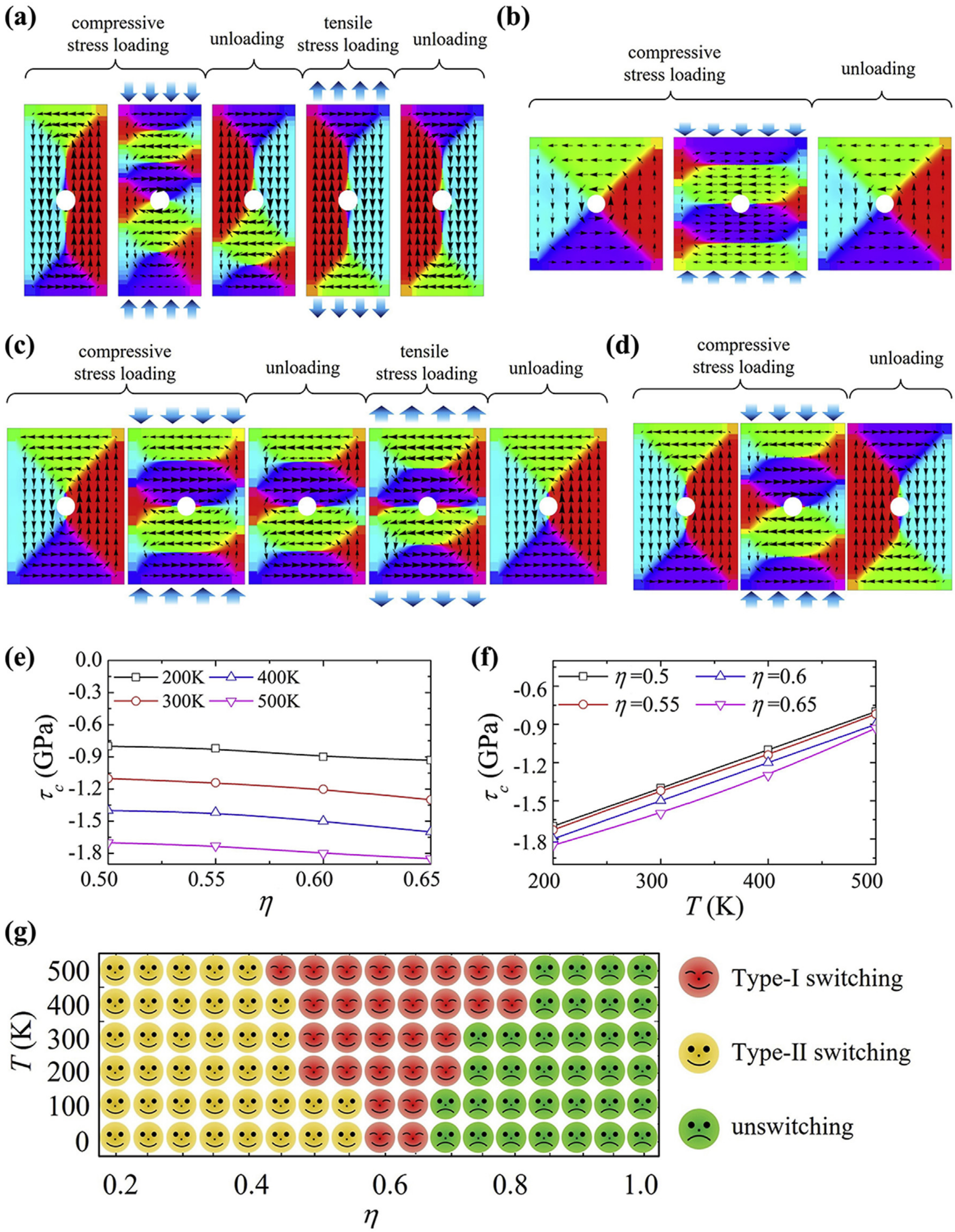

Fig. 8. Snapshots of the VDS evolution for four FNPLs with a void subjected to a compressive stress loading/unloading process at room temperature, with the width-length ratio η being (a) 0.4, (b) 1.0, (c) 0.8 and (d) 0.6. In (a) and (c), VDS evolution under a further tensile stress loading/unloading process is depicted. Critical surface traction τ_c of Type-I switching is plotted as a function of (e) width-length ratio and (f) temperature. (g) Phase diagram summarizing the feasibility of stress-induced vortex switching as a function of width-length ratio and temperature in FNPLs with a void at the center.

3-vortices state, which maintains stable after stress unloading (Fig. 8c). The stabilization of the 3-vortices state at zero stress reflects the delicate balance of the three vortices at this geometry. Interestingly, Type-II switching does not occur after a further application of tensile stress. Note that as the width-length ratio of FNPL increases, the multi-vortices state becomes more and more alike stripe domain pattern. Such a stripe feature may be responsible for failure of vortex switching. Moreover, for FNPL with $\eta = 1$, the single-vortex state evolves into a 3-vortices state and back to a single-vortex state. However, vortex switching does not occur. In this case, the vortex nucleation and annihilation region are the same, i.e., near the top and bottom surfaces. As the width-length ratio approaches one, the vortex around the void is rather stable, and the favored vortex nucleation region is changed to be near the surfaces.

The critical surface traction τ_c of Type-I switching is plotted as a function of width-length ratio and temperature in Fig. 8e and f, respectively. One can see that τ_c increases slightly as the width-length ratio increases at given temperature, whereas it decreases with the increase of temperature for given width-length ratio. Analogous to the above, we also draw a phase diagram about the feasibility of stress-induced vortex switching as a function of width-length ratio and temperature in FNPLs with a void at the center, as shown in Fig. 8g. From this diagram, we can conclude that mechanical switching is valid when the width-length ratio η lies between the value ranges from 0 to 0.8. Type-II switching occurs at smaller η and lower temperature, whereas Type-I switching is more important when η is larger and the temperature is higher. The vortex switching cannot be achieved if η is larger than 0.8 for the temperature range we investigated.

4.5. Effect of void position on vortex switching

The effect of void position on the feasibility of vortex switching in FNPLs with a void is further discussed in this section. As we have shown above, the void enhances the stability of the vortex rotating around it. Vortices tend to nucleate around the void but annihilate away from the void. As the favored vortex nucleation and annihilation regions are not the same, a deterministic switching of vortex chirality by stress can be achieved. Obviously, the enhancing effect of the void on stability of nucleated vortex should be only applicable when the void position is compatible with the geometrically

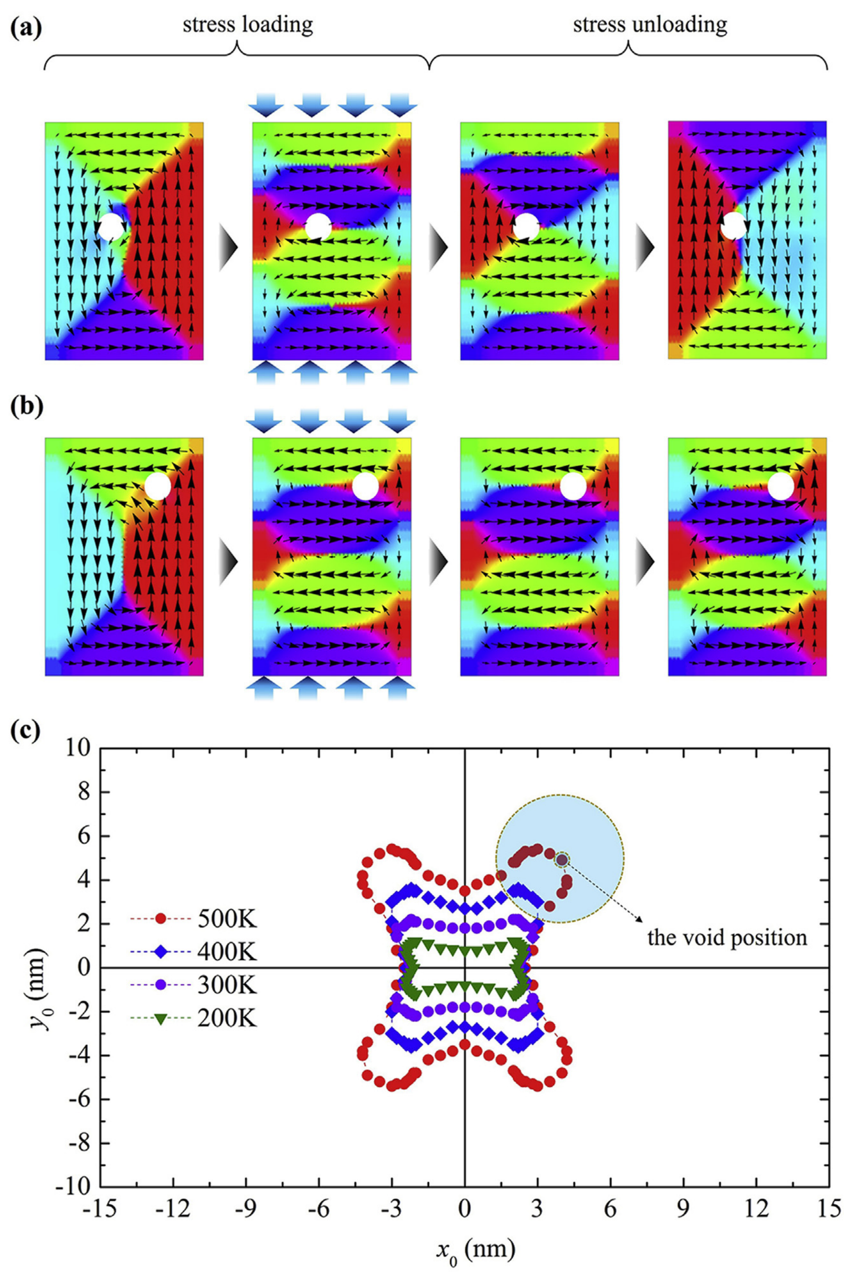

Fig. 9. Snapshots of the VDS evolution for two FNPLs with void center located at (a) (2 nm, 2 nm) and (b) (10 nm, −5 nm). (c) Phase diagram summarizing the feasibility of Type-I switching as a function of void position and temperature.

favored vortex nucleation point. In particular, for FNPLs with the default geometry studied in this work, the geometrically favored vortex nucleation point is the center of the FNPL. If the void position is too far away from the FNPL center, the void will not be a favored nucleation site of new vortex. As a consequence, stability of the new vortex will be only slightly enhanced or even decreased by the void, leads to the failure of a deterministic switching of vortex chirality by stress.

For simplicity, we focus on the effect of void position on the feasibility of Type-I switching in FNPLs subjected to a stress loading/unloading process at $T = 300$ K. The loading stress τ is chosen to be -3.0 GPa for all the FNPLs. Snapshots of the VDS evolution for two FNPLs with void center located at $(x_0, y_0) = (2$ nm, 2 nm$)$ and $(10$ nm, -5 nm$)$ are shown in Fig. 9a and b, respectively. One can see that while Type-I switching occurs for the first FNPL as the void is near the center of the FNPL, Type-I switching does not occur for the second FNPL. In the latter FNPL, the void is too far away from the center of the FNPL, but near the top surface. As a result, it stabilize not the vortex nucleated at the center but the vortex at the top surface, leading to the stabilization of a 3-vortices state in the FNPL after the stress unloading. To have a clear insight into the void position effect, we systematically inspect the feasibility of Type-I switching as a function of void position and temperature and summarize a phase diagram as shown in Fig. 9c. Here, each pair of (x_0, y_0) coordinates, with the value limited in the region the FNPL, corresponds to a position of the void in FNPL. The temperature is ranging from 200 K to 500 K. It can be seen that for each temperature point, the switchable region is a butterfly-like region. As the temperature increases, the switchable region gets larger. The large switchable region is of practical significance as it means we do not need to precisely control the void position in the FNPL to obtain Type-I switching.

5. Discussion

At the end of the part, we would like to use a schematic to discuss the feasibility of stress-induced vortex switching in FNPLs. Firstly, to realize such a switching, vortex multiplication with the appearance of 'new' vortex (vortices) with opposite chirality to the initial vortex is necessary. Secondly, vortex annihilation with the disappearance of 'old' vortex (vortices) with the same chirality to the initial vortex is also necessary. As shown in Fig. 10a and b, both FNPLs without or with a void would undergo vortex multiplication under a compressive stress, as indicated by paths A→B and A'→B′, with A (A′) denoting the initial single-vortex state and B (B′) the multi-vortices state at compressive stress. However, for FNPL without void, stability of 'new' vortex (vortices) with opposite chirality to the initial vortex is expected to be weaker than that of 'old' vortex (vortices) with the same chirality to the initial vortex, since there are no sources that can bias the 'new' vortex (vortices) to be more stable than the 'old' vortex (vortices). The 'new' vortex (vortices) become unstable after the removal of compressive stress (B→A), or although they maintain stable after the removal of compressive stress (B→C) but become unstable when further subjected to a tensile stress (C→D), with C denoting the multi-vortices state at zero stress and D the single-vortex state at tensile stress. As the 'old' vortex (vortices) are always dominant over the 'new' vortex (vortices), neither route A→B→A and A→B→C→D→A can lead to vortex switching (Fig. 10a). In contrast, for FNPLs with a void, the void can enhance the relative stability of the 'new' vortex (vortices) with opposite chirality to the initial vortex, as the void can remove the high energy of vortex core. In other words, the void is like a bias source that can make the vortex around it more stable. As a result, the 'old' vortex (vortices) with the same chirality to the initial vortex become unstable after the removal of compressive stress (B'→E′), or although they maintain stable after the removal of compressive stress (B'→C′) but become unstable when further subjected to a tensile stress (C'→D′). Here C′, D′ and E′ denote the multi-vortices state at zero stress, the single-vortex state at tensile stress, and the single-vortex state with opposite chirality to the initial state at zero stress, respectively. Both routes A'→B'→E′ and A'→B'→C'→D'→E′ can lead to vortex switching (Fig. 10b). Specially, Type-I switching are along the route A'→B'→E′ where only compressive stress is necessary. Meanwhile, Type-II switching, which requires a combined application of compressive and tensile stress, are along the route A'→B'→C'→D'→E'.

In the process of stress-induced vortex switching, the enhanced stability of vortex around the void defect is the key factor. In principle, other defects in ferroelectric nanostructures, such as

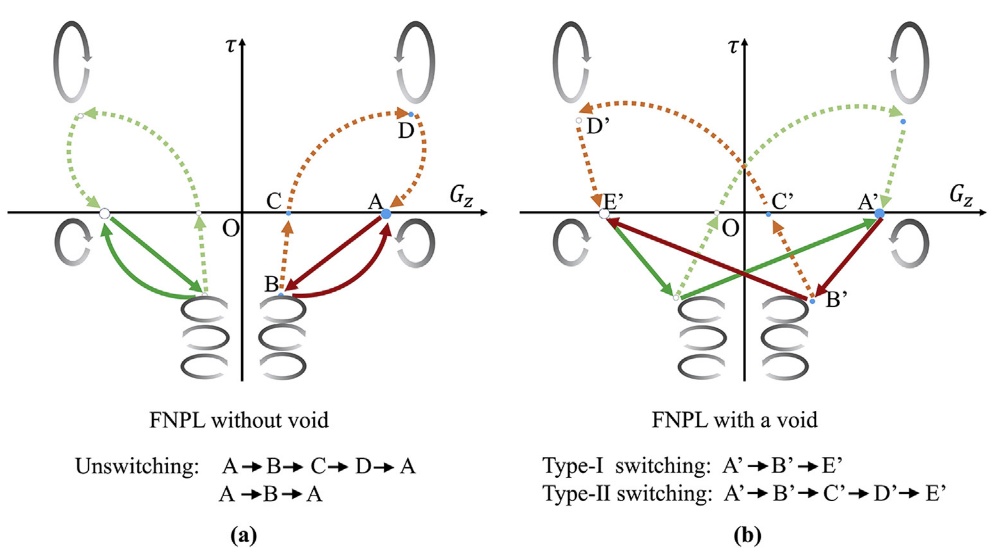

Fig. 10. A schematic summarizing the feasibility of stress-induced vortex switching in FNPLs. (a) Vortex switching does not occur in FNPL without void after stress-induced vortex multiplication and annihilation processes A→B→A and A→B→C→D→A. In contrast, (b) Type-I switching and Type-II switching process can occur in FNPL with a void after stress-induced vortex multiplication and annihilation processes A'→B'→E′ and A'→B'→C'→D'→E'.

dislocation lines, immobile charge defects, and local surface rumplings, etc., are expected to affect the dipole behavior nearby and consequently modify the stress-induced vortex multiplication and annihilation behaviors of the overall system. In addition to voids, these defects should be also promising sources that can facilitate mechanical switching of ferroelectric vortex.

6. Summary

In ferroelectrics, owing to electrostrictive effect, the magnitude and orientation of polar dipoles can be modulated mechanically. In this work, we introduce a void defect into FNPL, and systematically investigate the influence of a void on the formation and transformation behaviors of VDS. It is found that stabilization of single-vortex state is enhanced and vortex switching by stress becomes feasible. This is due to that the void is like a bias source that can make the vortex around it more stable, and consequently, the stress-induced vortex multiplication and annihilation behaviors are modified by the void. Furthermore, we systematically discuss the effects of various factors on feasibility of stress-induced vortex switching including temperature, void size, width-length ratio of FNPL, and void position in FNPL. Fruitful phase diagrams are summarized. Our results elucidate the feasibility of vortex switching by stress, and should be instructive for the practical control and applications of ferroelectric VDS.

Acknowledgements

The authors acknowledge support from NSFC (Nos. 11672339, 11474363, 11572355, 11602310, 11232015). Yue Zheng also acknowledges the support from the Special Program for Applied Research on Super Computation of the NSFC Guangdong Joint Fund, the Fok Ying Tung Foundation, the Guangdong Natural Science Funds for Distinguished Young Scholar and the China Scholarship Council.

References

[1] I.I. Naumov, L. Bellaiche, H. Fu, Unusual phase transitions in ferroelectric nanodisks and nanorods, Nature(London UK) 432 (2004) 737–740.
[2] A. Gruverman, D. Wu, H.-J. Fan, I. Vrejoiu, M. Alexe, R.J. Harrison, J.F. Scott, Vortex ferroelectric domains, J. Phys. Condens. Matter 20 (2008) 7260–7265.
[3] B.J. Rodriguez, X.S. Gao, L.F. Liu, W. Lee, I.I. Naumov, A.M. Bratkovsky, D. Hesse, M. Alexe, Vortex polarization states in nanoscale ferroelectric arrays, Nano Lett. 9 (2009) 1127–1131.
[4] Y. Ivry, D.P. Chu, J.F. Scott, C. Durkan, Flux closure vortexlike domain structures in ferroelectric thin films, Phys. Rev. Lett. 104 (2010), 207602.
[5] C.L. Jia, K.W. Urban, M. Alexe, D. Hesse, I. Vrejoiu, Direct observation of continuous electric dipole rotation in flux-closure domains in ferroelectric $Pb(Zr,Ti)O_3$, Science 331 (2011) 1420–1423.
[6] Y. Zheng, W.J. Chen, Characteristics and controllability of vortices in ferromagnetics, ferroelectrics and multiferroics, Rep. Prog. Phys. 80 (2017), 086501.
[7] Z. Li, Y. Wang, G. Tian, P. Li, L. Zhao, F. Zhang, J. Yao, H. Fan, X. Song, D. Chen, Z. Fan, M. Qin, M. Zeng, Z. Zhang, X. Lu, S. Hu, C. Lei, Q. Zhu, J. Li, X. Gao, J. Liu, High-density array of ferroelectric nanodots with robust and reversibly switchable topological domain states, Science Advances 3 (2017), e1700919.
[8] J.M. Gregg, Exotic domain states in ferroelectrics: searching for vortices and skyrmions, Ferroelectrics 433 (2012) 74–87.
[9] M.G. Stachiotti, M. Sepliarsky, Toroidal ferroelectricity in $PbTiO_3$ nanoparticles, Phys. Rev. Lett. 106 (2011), 137601.
[10] C.M. Wu, W.J. Chen, Y. Zheng, D.C. Ma, B. Wang, Y.L. Liu, C.H. Woo, Controllability of vortex domain structure in ferroelectric nanodot: fruitful domain patterns and transformation paths, Sci. Rep. 4 (2014) 3946.
[11] S. Prosandeev, I. Ponomareva, I. Kornev, I. Naumov, L. Bellaiche, Controlling toroidal moment by means of an inhomogeneous static field: an *Ab Initio* study, Phys. Rev. Lett. 96 (2006), 237601.
[12] I. Naumov, H. Fu, Vortex-to-Polarization phase transformation path in ferroelectric $Pb(ZrTi)O_3$ nanoparticles, Phys. Rev. Lett. 98 (2007), 077603.
[13] I. Naumov, H. Fu, Cooperative response of $Pb(ZrTi)O_3$ nanoparticles to curled electric fields, Phys. Rev. Lett. 101 (2008), 197601.
[14] W.J. Chen, Y. Zheng, B. Wang, Vortex domain structure in ferroelectric nanoplatelets and control of its transformation by mechanical load, Sci. Rep. 2 (2012) 796.
[15] W.J. Chen, Y. Zheng, B. Wang, Phase field simulations of stress controlling the vortex domain structures in ferroelectric nanosheets, Appl. Phys. Lett. 100 (2012), 062901.
[16] X. Fu, I.I. Naumov, H. Fu, Collective dipole behavior and unusual morphotropic phase boundary in ferroelectric Pb $(Zr_{0.5}Ti_{0.5})O_3$ nanowires, Nano Lett. 13 (2013) 491–496.
[17] W.J. Chen, Y. Zheng, B. Wang, Large and tunable polar-toroidal coupling in ferroelectric composite nanowires toward superior electromechanical responses, Sci. Rep. 5 (2015), 11165.
[18] V.M. Dubovik, V.V. Tugushev, Toroid moments in electrodynamics and solid-state physics, Phys. Rep. 187 (1990) 145–202.
[19] S. Prosandeev, I. Ponomareva, I. Kornev, L. Bellaiche, Control of vortices by homogeneous fields in asymmetric ferroelectric and ferromagnetic rings, Phys. Rev. Lett. 100 (2008), 047201.
[20] W.J. Chen, Y. Zheng, B. Wang, J.Y. Liu, Coexistence of toroidal and polar domains in ferroelectric systems: a strategy for switching ferroelectric vortex, J. Appl. Phys. 115 (2014), 214106.
[21] W.J. Chen, Y. Zheng, Vortex switching in ferroelectric nanodots and its feasibility by a homogeneous electric field: effects of substrate, dislocations and local clamping force, Acta Mater. 88 (2015) 41–54.
[22] X. Ren, Large electric-field-induced strain in ferroelectric crystals by point-defect-mediated reversible domain switching, Nat. Mater. 3 (2004) 91–94.
[23] J.F. Scott, C.A. Araujo, Ferroelectric memories, Science(Washington, D. C.) 246 (1989) 1400–1405.
[24] C.A.P. de Araujo, J.D. Cuchiaro, L.D. McMilian, M.C. Scott, J.F. Scott, Fatigue-free ferroelectric capacitors with platinum electrodes, Nature 374 (1995) 627–629.
[25] J.F. Scotta, M. Dawber, Oxygen-vacancy ordering as a fatigue mechanism in perovskite ferroelectrics, Appl. Phys. Lett. 76 (2000) 3801–3803.
[26] A.K. Tagantsev, Landau expansion for ferroelectrics: which variable to use? Ferroelectrics 375 (2008) 19–27.
[27] Y. Zheng, C.H. Woo, Thermodynamic modeling of critical properties of ferroelectric superlattices in nano-scale, Appl. Phys. A 97 (2009) 617–626.
[28] C.H. Woo, Y. Zheng, Depolarization in modeling nano-scale ferroelectrics using the Landau free energy functional, Appl. Phys. A 91 (2008) 59–63.
[29] J.J. Wang, X.Q. Ma, Q. Li, J. Britson, L.Q. Chen, Phase transitions and domain structures of ferroelectric nanoparticles: phase field model incorporating strong elastic and dielectric inhomogeneity, Acta Mater. 61 (2013) 7591–7603.
[30] W.J. Chen, Y. Zheng, B. Wang, D.C. Ma, F.R. Ling, Vortex domain structures of an epitaxial ferroelectric nanodot and its temperature-misfit strain phase diagram, Phys. Chem. Chem. Phys. 15 (2013) 7277–7285.
[31] J. Hlinka, P. Marton, Phenomenological model of a 90° domain wall in Ba Ti O 3-type ferroelectrics, Phys. Rev. B 74 (2006), 104104.
[32] A.G. Khachaturyan, Theory of Structure Transformations in Solids, Wiley, New York, 1983.
[33] N.A. Pertsev, A.G. Zembilgotov, A.K. Tagantsev, Effect of mechanical boundary conditions on phase diagrams of epitaxial ferroelectric thin films, Phys. Rev. Lett. 80 (1998) 1988–1991.
[34] K. Ishikawa, T. Uemori, Surface relaxation in ferroelectric perovskites, Phys. Rev. B 60 (1999), 11841.
[35] L.D. Landau, E.M. Lifshitz, L.P. Pitaevskii, Electrodynamics of Continuous Media, Oxford University Press, Oxford, 1984.
[36] A.K. Tagantsev, G. Gerra, N. Setter, Short-range and long-range contributions to the size effect in metal-ferroelectric-metal heterostructures, Phys. Rev. B 77 (2008) 174111.
[37] a_1=3.85(T-752)×10^5, a_{11}=-7.3×10^7, a_{12}=7.5×10^8, a_{111}=2.6×10^8, a_{112}=6.1×10^8, a_{123}=-3.7×10^9, C_{11}=1.746×10^{11}, C_{12}=0.7937×10^{11}, C_{44}=1.1111×10^{11}, Q_{11}=0.089, Q_{12}=-0.026, Q_{44}=0.0675, G_{11}=3.46×10^{-10}, G_{12}=0, G_{44}=1.73×10^{-10}, $G_{14}=G_{12}+G_{44}$, D_i^S=3.46×10^{-10}, δ_i^{eff}=5×10^{-9}, ε_b=4.425×10^{-10}(in SI units).
[38] J. Wang, J. Zhang, T. Shimada, T. Kitamura, Effect of strain on the evolution of magnetic multi-vortices in ferromagnetic nano-platelets, J. Phys. Condens. Matter 25 (2013) 226002.
[39] Q. Sheng, X.L. Liu, W.J. Chen, W.M. Xiong, G.L. Jiang, Y. Zheng, Domain stability and polar-vortex transformations controlled by mechanical loads in soft ferromagnetic nanodots, AIP Adv. 6 (2016), 035003.
[40] M. Kläui, C.A.F. Vaz, L. Lopez-Diaz, J.A.C. Bland, Vortex formation in narrow ferromagnetic rings, J. Phys. Condens. Matter 15 (2003) R985–R1023.
[41] C.A. Vaz, T.J. Hayward, J. Llandro, F. Schachert, D. Morecroft, J.A.C. Bland, M. Kläui, M. Laufenberg, D. Backes, U. Rüdiger, F.J. Castaño, C.A. Ross, L.J. Heyderman, F. Nolting, A. Locatelli, G. Faini, S. Cherifi, W. Wernsdorfer, Ferromagnetic nanorings, J. Phys. Condens. Matter 19 (2007), 255207.